Pressure-tuned valence transition, insulator-metal transition in van der Waals antiferromagnet $CrPS_3$

Dipayan Sen and Tanusri Saha-Dasgupta*

Department of Condensed Matter and Materials Physics, S. N. Bose National Centre for Basic Sciences, JD Block, Sector III, Salt Lake, Kolkata 700106, India

(Received 4 April 2023; revised 25 May 2023; accepted 20 June 2023; published 30 June 2023)

Motivated by the recent reports of pressure-induced engaging phenomena in van der Waals antiferromagnetic late transition metal phosphorous trisulfide compounds such as $FePS_3$, $NiPS_3$, and $MnPS_3$, we explore the effect of pressure in an early-transition-metal-based compound, $CrPS_3$. Our study, combining an evolutionary algorithm and first-principles calculations, establishes the existence of a pressure-induced insulator-metal transition in $CrPS_3$ akin to that in $FePS_3$, $NiPS_3$, and $MnPS_3$. However, while for late-transition-metal-based compounds such as $FePS_3$ and $MnPS_3$ the application of pressure causes a spin-state transition, in an early-transition-metal-based system it causes a valence transition, driven by the destabilization of P-P dimerization. The weakening of metal-sulfur covalency in early transition metals compared with late transition metals is found to be the origin of this contrasting behavior. The high-pressure phase is predicted to exhibit easy-axis, in-plane ferromagnetism, opening the possibility of realizing two-dimensional ferromagnetism in this class of compounds.

DOI: 10.1103/PhysRevMaterials.7.064008

I. INTRODUCTION

Since the sensational discovery of graphene, a monatomic layer of carbon atoms, a variety of two-dimensional (2D) materials have been synthesized [1]. While a number of exciting phenomena have been reported in 2D, such as unprecedented carrier mobility, charge-density-wave, superconductivity, and topological properties, until recently missing from the 2D portfolio was the intrinsic magnetic order. The discovery of intrinsic ferromagnetism in 2D van der Waals crystals such as $Cr_2Ge_2Te_6$ [2] and CrI_3 [3] was therefore met with huge excitement. Since then, two-dimensional van der Waals magnets have been the focus of attention [4]. Weak van der Waals (vdW) interlayer interactions between adjacent layers in these compounds provide an appealing platform for studying the interplay between various versatile electronic and magnetic phenomena in low dimensions. Interestingly, most such magnets are found to have an underlying hexagonal or triangular lattice. The layered transition metal hexagonal lattices include binary transition metal trihalides MX_3 (M = Cr, V, or Ni; X is a halide) [5], MPS_3 (M = Mn, Fe, or Ni) [6], and $Cr_2Z_2Te_6$ (Z = Si or Ge) [7]. Triangular lattice magnets include systems such as Fe_3GeTe_2 [8], $MnBi_{2n}Te_{3n+1}$ [9], and prismatic (2H) or octahedral (1T) binary transition metal dichalcogenides such as AY_2 (A = V, W, or Mo; Y = S or Se) [10].

In this paper, we focus on the hexagonal MPS_3 family, which has been studied quite extensively both experimentally and computationally. The crystal structure of this family of compounds consists of a honeycomb network of transition metal (M) cations, which are van der Waals stacked in an AAA sequence. The dumbbell-shaped $(P_2S_6)^{-4}$ molecular unit, formed by a P-P dimer with three S atoms connected to each P, passes through the center of each honeycomb lattice hexagon, aligned perpendicular to the hexagonal plane [cf. Fig. 1(a)]. The M-atom hexagonal lattice and the molecular complexes are connected through shared S atoms, with M atoms in octahedral coordination with S atoms [11]. Compounds with magnetic M ions such as Fe, Ni, or Co, as well as nonmagnetic M ions such as Zn or Cd, have been synthesized [12]. The magnetic ground state in all cases in which M is a magnetic ion turned out to be antiferromagnetic. The precise nature of in-plane antiferromagnetic order is found to be determined by the complex interplay between first-, second-, and third-neighbor M-M interactions, which can stabilize Neél antiferromagnetism (AFM), stripe antiferromagnetism (SAFM), or zigzag antiferromagnetism (ZAFM) [cf. Fig. 1(b)] [13]. While $CoPS_3$, $FePS_3$, and $NiPS_3$ stabilize in a SAFM structure, $MnPS_3$ stabilizes in an AFM structure. The out-of-plane magnetic interaction, which is generally an order of magnitude or more smaller compared with in-plane magnetic interactions, can be ferromagnetic (FM) or AFM. For $CoPS_3$, $MnPS_3$, and $NiPS_3$, the out-of-plane interaction is found to be FM, while for $FePS_3$ it is found to be AFM [12]. It is an interesting question to ask whether these antiferromagnetic van der Waals compounds can be turned into ferromagnets, as the most sought-after 2D magnetic configuration for practical applications is ferromagnetism.

In this context, tuning of physical properties by external perturbation, namely, hydrostatic pressure, has also been studied in this interesting family of compounds [14]. As expected, the application of hydrostatic pressure will push the layers close to each other, finally closing the van der Waals gap. A pressure-induced insulator-to-metal transition, together with a transition of Fe^{2+} from high spin, $S = 2$, to low spin, $S = 0$, has been reported for $FePS_3$ [15]. Subsequent

*t.sahadasgupta@gmail.com

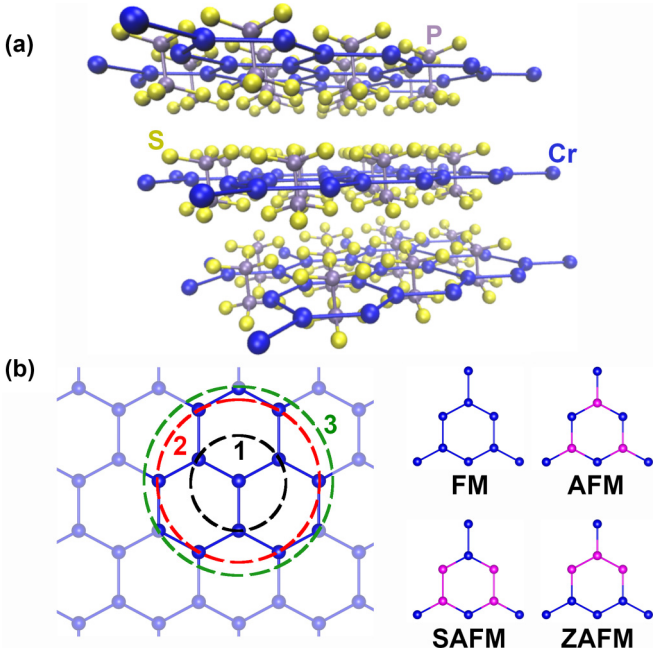

FIG. 1. (a) Ambient-pressure crystal structure of MPS_3 in the monoclinic $C2/m$ space group with AAA stacking of hexagonal M layers and (P_2S_6) molecular units. (b) The nearest-neighbor (1), second-nearest-neighbor (2), and third-nearest-neighbor (3) in-plane magnetic interactions in the transition metal sublattice, and possible in-plane magnetic orderings: ferromagnetic (FM), Néel antiferromagnetic (AFM), stripe AFM (SFM), and zigzag AFM (ZFAM). The two different colors of the balls denote the up and down directions of the M spin.

measurements have also revealed superconductivity in the high-pressure phase of $FePS_3$ [16]. Pressure-induced dimensionality crossover and an insulator-to-metal transition have also been observed in $NiPS_3$ [17] and $MnPS_3$ [18]. Interestingly, all the above compounds concern the cases where the M site is a late transition metal. Apart from some partial investigation of the transition-metal-deficient compound $V_{0.9}PS_3$, there are not many reports on early transition metal compounds. Motivated by the pioneering examples of 2D magnetism in CrI_3 and $Cr_2Ge_2Te_6$, in this paper we focus on the case of $M = Cr$. Cr-based layered transition metal phosphorous trichalcogenides have been studied for their water absorption and electrochemical activity [19]. Although synthesis of $CrPS_3$ under ambient conditions has not been reported, synthesis of the related compound $CrPSe_3$ has been reported [20]. Using first-principles calculations, we first study the magnetic and electronic properties of $CrPS_3$ under ambient conditions and compare it with other transition-metal-based phosphorous trichalcogenides such as $FePS_3$, $MnPS_3$, and $NiPS_3$. Following this, we explore the influence of pressure. Employing a genetic algorithm, we characterize the high-pressure phases and uncover the pressure-driven structural transitions. Similar to $FePS_3$, $NiPS_3$, and $MnPS_3$, an insulator-to-metal transition is found for $CrPS_3$. However, remarkably, while the insulator-to-metal transition in $FePS_3$ ($MnPS_3$) is accompanied by a spin-state transition of Fe (Mn), for $CrPS_3$ the insulator-to-metal transition is found to be accompanied, in contrast, by a valence transition of Cr. The origin of pressure-induced change of the oxidation state of Cr is found to be connected to pressure-driven destabilization of P-P dimerization, resulting in change in the valence of the (P_2S_6) unit. This bears a resemblance to the recent discussion pertaining to the unexpected valence of Fe in the high-pressure compound FeO_2 [21]. Interestingly, the high-pressure metallic phase is found to host easy-axis, in-plane ferromagnetism, raising interest in this unexplored compound. We close our study answering why early-transition-metal-based phosphorous trichalcogenides such as $CrPS_3$ behave differently from late-transition-metal-based phosphorous trichalcogenides such as $FePS_3$.

II. COMPUTATIONAL METHODOLOGY

We used first-principles calculations to study different properties of the proposed $CrPS_3$ compounds. Structural relaxations and total energy computations were performed using the Vienna *ab initio* simulation package (VASP) [22,23], which employs plane-wave density functional theory (DFT) and projector-augmented wave (PAW) [24] potentials. An exchange correlation functional based on the generalized gradient approximation (GGA) of Perdew-Burke-Ernzerhof [25] type was used in all calculations. GGA level computations were further supplemented by Dudarev *et al.*'s [26] GGA + U approach to account for electronic correlation effects at the Cr sites. Within the Dudarev formalism of GGA+U for multiorbital models, the value of "U-J" was chosen to be 4 eV. The obtained results were checked in terms of variation of the U-J value by 1–2 eV. The van der Waals interaction was included in the calculations using Grimme's [27] empirical dispersion correction within the DFT+D2 formulation.

For ionic and cell relaxations, all systems were allowed to relax till forces became less than 0.0001 eV/Å. For describing various magnetic states, 2×1×2 supercells of the conventional unit cell of the monoclinic phases and 2×2×2 supercells of the conventional unit cell of the trigonal phase were used. An energy cutoff of 1200 eV and an 8×8×8 Monkhorst-Pack k-point mesh were found to provide good convergence of the total energy in the chosen systems and were thus used in all calculations. The phonon dispersion calculations to probe the dynamical stability were carried out using PHONOPY [28,29]. The thermal stability was estimated using *ab initio* molecular dynamics (AIMD) computations as implemented in VASP. To this end, an N-V-T ensemble is considered, and using a Nosé-Hoover [30] thermostat, the DFT-predicted structure(s) was maintained at 300 K for up to 20 ps with 1-fs time step.

The ambient- as well as high-pressure phases of $CrPS_3$ were searched for using Universal Structure Predictor: Evolutionary Xtallography (USPEX) [31–33], an evolutionary crystal structure prediction algorithm, in conjunction with VASP.

III. RESULTS AND DISCUSSION

A. Ambient-pressure phase

1. Structure and stability

We used the USPEX implementation [31–33] of the evolutionary algorithm for crystal structure prediction, which

mimics Darwinian evolution and employs a natural selection of the fittest in combination with variation operators, to predict the crystal structure of the yet-to-be-synthesized ambient-pressure phase of $CrPS_3$. Three-dimensional bulk MPX_3 ($X = S, Se$) crystals usually adopt either an AAA stacking in the $C2/m$ space group or an ABC stacking in the $R\text{-}3$ space group, both of which can be represented in a hexagonal unit cell containing three MPX_3 single layers having D_{3d} symmetry, which are stacked in a different way. The evolutionary-algorithm-predicted $CrPS_3$ crystal structure turned out to be $C2/m$, the same as that of $FePS_3$, $CoPS_3$, $MnPS_3$, and $NiPS_3$. The crystal structure of $CrPS_3$, given by USPEX, was further fully relaxed by fixing the symmetry, in nonmagnetic, ferromagnetic, and three different antiferromagnetic arrangements of the Cr spins, to take into account possible magnetostructural coupling. The structural parameters turned out to be strongly dependent on the chosen spin arrangements, suggestive of strong magnetostructural coupling. The energetically most favorable spin arrangement turned out to be Néel AFM order. The a and c lattice parameters of $CrPS_3$ are found to show an increase of $\sim$3% compared with those of $FePS_3$ in their respective ground-state magnetic arrangements, while the b lattice parameter and monoclinic angle are found to exhibit marginal change.

In order to ascertain the stability of the predicted $CrPS_3$ structure, we calculated the formation energy, given by the expression $H_f = E(CrPS_3) - (\mu_{Cr} + \mu_P + 3\mu_S)$, where $E(CrPS_3)$ is the total energy of the corresponding $CrPS_3$ phase, and μ_{Cr}, μ_P, and μ_S are the chemical potentials of the corresponding elements. Following the Open Quantum Materials Database [34], the chemical potentials are taken as total energies per atom of elemental bcc Cr crystal, β-phosphorous in triclinic crystal, and β-sulfur in monoclinic crystal. The calculations show the stability of $CrPS_3$ (-0.39 eV/atom) to be comparable to that of $FePS_3$ (-0.37 eV/atom) and $NiPS_3$ (-0.36 eV/atom). Molecular dynamics simulations at room temperature (300 K) also show good thermal stability of the structure at room temperature [Fig. 2(a)]. $CrPS_3$ is further found to be lattice dynamically stable, as shown by the calculated phonon spectrum in Fig. 2(b), where no imaginary frequencies are found.

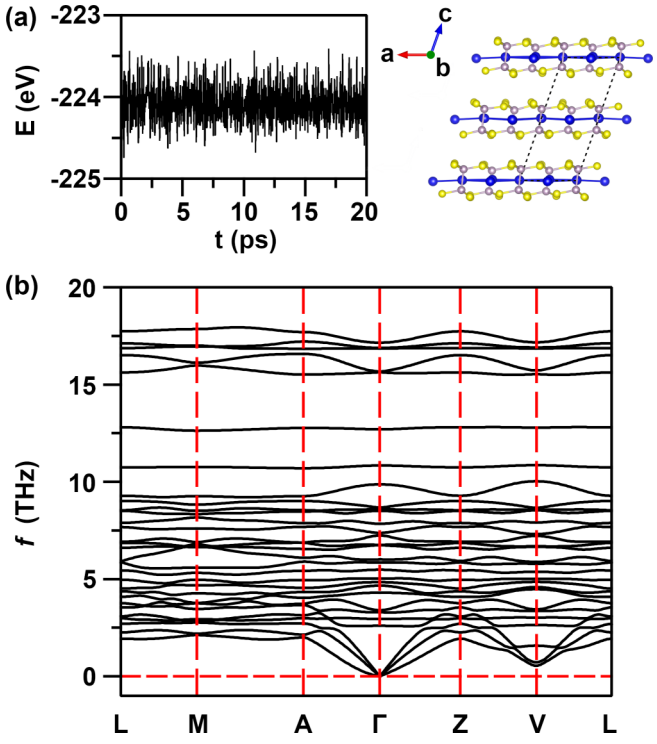

FIG. 2. (a) Molecular dynamics simulation at room temperature on the ambient-pressure structure (shown on the right) for 20 ps, showing good thermal stability. (b) Calculated phonon spectrum, plotted along the high-symmetry points of the monoclinic Brillouin zone, showing no imaginary frequencies, indicating that the structure is lattice dynamically stable.

2. *Magnetic order, magnetic exchanges, and anisotropy*

Magnetic exchange energies of the $CrPS_3$ compound were evaluated by calculating total energies within the GGA+U+D2 scheme of eight different magnetically ordered configurations: $E_{FM,FM}$, $E_{FM,AFM}$, $E_{AFM,FM}$, $E_{AFM,AFM}$, $E_{SAFM,FM}$, $E_{SAFM,AFM}$, $E_{ZAFM,FM}$, and $E_{ZAFM,AFM}$, where the first term in the subscript refers to the in-plane magnetic ordering and the second term in the subscript refers to the out-of-plane magnetic ordering. FM, AFM, SAFM, and ZAFM denote ferromagnetic, Néel antiferromagnetic, S-type antiferromagnetic, and Z-type antiferromagnetic ordering, as mentioned before. The details of spin arrangements in the FM and different AFM phases, along with total energies, can be found in the Supplemental Material [38]. Subsequently, total energies were mapped into the Hamiltonian $H = -\frac{1}{2}\sum_{i\neq j} J_{ij}\vec{S}_i \cdot \vec{S}_j$, where J_{ij} denotes magnetic exchanges between i and j sites and $\vec{S}_i$ and $\vec{S}_j$ denote the spin magnetic moment at i and j sites, respectively. Considering three in-plane nearest neighbors and one out-of-plane nearest neighbor, the corresponding magnetic exchange energies for bulk $CrPS_3$ at 0 GPa were solved as

$$J_1 = -\frac{1}{32S^2}[(E_{FM,AFM} - E_{AFM,AFM}) - (E_{SAFM,AFM} - E_{ZAFM,AFM})],$$

$$J_2 = -\frac{1}{64S^2}[E_{FM,AFM} + E_{AFM,AFM} - E_{SAFM,AFM} - E_{ZAFM,AFM}],$$

$$J_3 = -\frac{1}{96S^2}[(E_{FM,AFM} - E_{AFM,AFM}) + 3\times(E_{SAFM,AFM} - E_{ZAFM,AFM})],$$

$$J_o = -\frac{1}{16S^2}[E_{ZAFM,FM} - E_{ZAFM,AFM}],$$

where $J>0$ ($J<0$) implies ferromagnetic (antiferromagnetic) exchange.

Figure 3 shows the computed values of three in-plane magnetic exchanges, J_1, J_2, J_3, and the out-of-plane magnetic exchange J_o for $CrPS_3$, $FePS_3$, $MnPS_3$, and $NiPS_3$. For $FePS_3$, $MnPS_3$, and $NiPS_3$, the available experimental estimates obtained from inelastic neutron scattering are also shown in the figure. We find that the agreement between our calculated values and experimental estimates is rather good, considering the small and delicate nature of magnetic exchanges. We

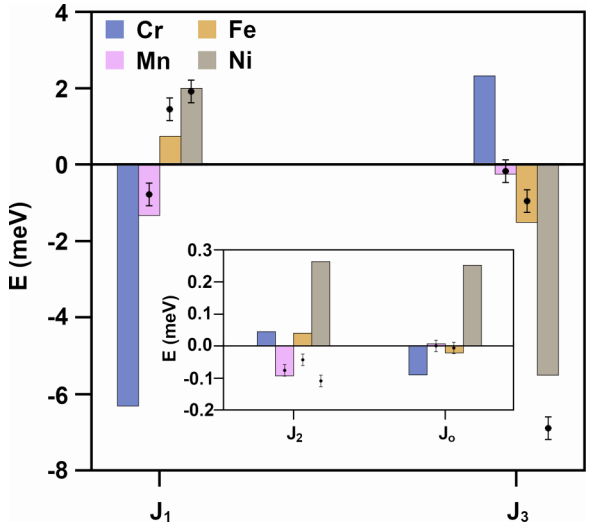

FIG. 3. Calculated values of three in-plane magnetic exchanges, J_1, J_2, J_3, and the interlayer magnetic interaction, J_o, for $CrPS_3$, in comparison to those of $FePS_3$, $MnPS_3$, and $NiPS_3$. Also shown are magnetic exchanges obtained from neutron scattering (black symbols), wherever available [35–37].

note a mismatch in the sign between the computed and experimentally estimated J_2 value for $NiPS_3$. The value of J_2, though, is small, a fraction of 1 meV, pushing it to the limit of DFT accuracy. However, to investigate the issue further, we repeated the calculation within an alternative formulation of GGA+U, namely, the Liechtenstein formulation [39]. Use of the Liechtenstein formulation of GGA+U kept the sign of the small exchange parameter, J_2, unchanged, with a value of 0.19 meV in comparison to a value of 0.26 in the Dudarev formulation and experimental estimate of -0.11 meV. It is to be noted that even the experimental estimate of such small exchange parameters is not devoid of error. This justifies the goodness of our calculations. Similar to other studied compounds, in $CrPS_3$ also the in-plane J_1 and J_3 interactions are found to be dominant, almost an order of magnitude larger compared with J_2 and J_o. Our predicted magnetic exchanges may be validated in future experiments.

We also calculated the single-ion magnetic anisotropy, which is expected to play a crucial role in the magnetic ordering of low-dimensional systems. The easy-axis magnetic anisotropy of $FePS_3$ turned out to be large, with a value of 6.8 meV, while that of both $MnPS_3$ and $CrPS_3$ turned out to be relatively small, with values of $\sim$0.06 and $\sim$0.12 meV, respectively. $MnPS_3$ anisotropy is predicted to be easy-axis anisotropy, in agreement with experiment, while that of $CrPS_3$ is predicted to be easy-plane anisotropy.

B. Pressure effect

1. Structural phase transitions

Following the study on the ambient-pressure phase, we next proceed with the effect of hydrostatic pressure on $CrPS_3$. The crucial step involved in this context is the prediction of pressure-driven structural phase transition. The USPEX code allows one to predict the crystal structure with arbitrary P-T conditions by knowing only the chemical composition of the material. We thus use the genetic algorithm as implemented in USPEX for this purpose. This algorithm considers energy as a fitness parameter, and ground-state structure is obtained by comparing energies among a large number of competitive structures over a number of generations. In this paper, the energies were calculated within the *ab initio* framework employing the plane-wave basis. The basic steps of the algorithm are shown in Fig. 4(a). In the initial generation of the genetic algorithm, the structures may be generated randomly from all the space group symmetries, or some seed crystal structures can be used. The latter process narrows the search space and saves computation time. In our calculations, we considered all possible reported crystal structures of MPX_3 at ambient- and high-pressure phases. In the following generations, the structures were produced using different variational operators such as 40% structures using heredity operators, 20% offspring from lattice mutation, 10% from permutation, and the rest of the structures being generated randomly. We first applied the USPEX algorithm to the known and studied case of pressure-driven structural transitions in $FePS_3$. Our USPEX calculations successfully reproduced the ambient-pressure structure and two different high-pressure structures reported for $FePS_3$, thus giving confidence in the applied methodology.

The USPEX study on $CrPS_3$ resulted in the $C2/m$ ambient-pressure phase (phase B-I) discussed above and two high-pressure phases, phases B-II and B-III. The crystal symmetry of phase B-II is monoclinic $C2/m$, which is the same as that of phase B-I, with a change in monoclinic angle from 109° to 93°, while the crystal symmetry of phase B-III is found to be trigonal P-31m. The intermediate-pressure phase B-II and high-pressure phase B-III are similar to those reported for $FePS_3$ [15]. As in $FePS_3$, phase B-III exhibits a substantial reduction of $\sim$21% in the out-of-plane lattice parameter, forming interlayer P-P bonds. Due to the high pressure, phase B-III also shows a staggered arrangement of S atoms in each layer, as shown in Fig. 4(b).

The enthalpy difference (ΔH) of phases B-II and B-III with respect to phase B-I along with pressure is plotted in Fig. 5(a). The lower inset shows the corresponding change in volume. The critical pressure for the B-I–B-II transition (P_{c1}) is found to be $\sim$5 GPa, while that for the B-II–B-III transition (P_{c2}) is found to be 20 GPa, compared with 3.3 and 17 GPa, respectively, for $FePS_3$. Following the trend of $FePS_3$, the volume change associated with the B-I–B-II transition is found to be marginal (0.61%), while that for the B-II–B-III transition is found to be substantial (5.74%).

2. Pressure-dependent electronic and magnetic structures

The pressure-driven insulator-to-metal transition happens concomitantly to the B-II–B-III phase transition, as is evident from the plot of the band gap (ΔE_{BG}) in Fig. 5(b). The band gap in phase B-II is found to be direct, while it is found to be indirect in phase B-I. Thus an indirect-band-gap-to-direct-band-gap transition happens concomitantly with the B-I–B-II transition.

The evaluation of the lowest-energy magnetic structure [cf. Fig. 6(a)] shows that while in phases B-I and B-II the magnetic structure remains Néel AFM, for phase B-III it

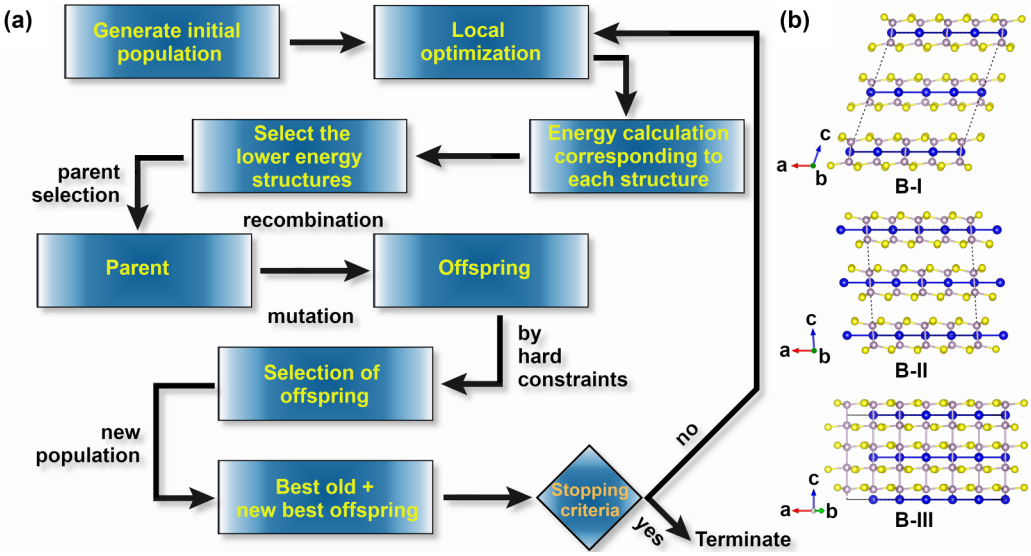

FIG. 4. (a) Flowchart of genetic algorithm for prediction of pressure-dependent crystal structures. (b) The predicted ambient-pressure phase (phase B-I) and two high-pressure phases (phases B-II and B-III). The colors of the balls representing the atoms are the same as in Fig. 1.

becomes in-plane FM with weak AFM interlayer coupling. Thus the high-pressure phase can serve as a host for the sought-after two-dimensional ferromagnetic system. This proposal becomes even more appealing owing to the fact that the magnetic anisotropy turns out to be an easy axis of non-negligible anisotropy of 0.20 meV.

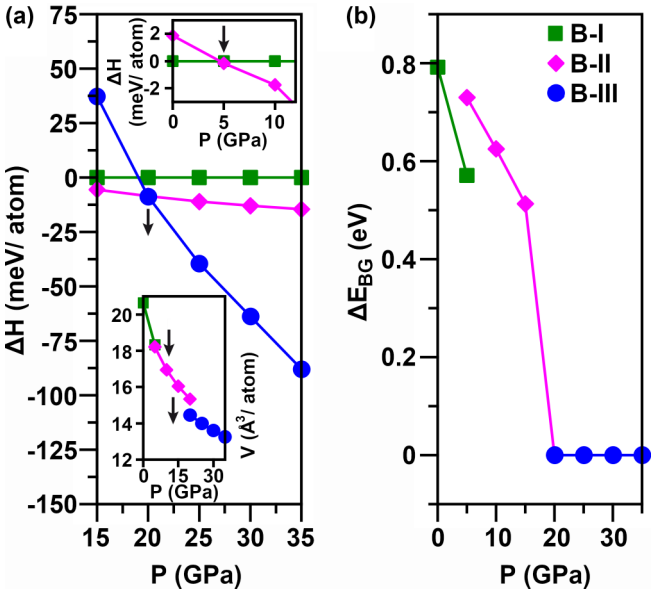

FIG. 5. (a) Enthalpy differences, relative to the phase B-I structure (green squares), of the phase B-II (magenta diamonds) and phase B-III (blue circles) structures, plotted as a function of pressure. The top inset shows the phase transition from phase B-I to phase B-II at low pressure. The arrows mark the critical pressures corresponding to structural transitions. The derived unit cell volume as a function of applied pressure for phases B-I, B-II, and B-III is shown in the lower inset. (b) The variation of the band gap, plotted as a function of pressure. The insulator-metal transition happens at 20 GPa.

Figure 6(b) shows the evolution of the magnetic moment at the Cr site as a function of pressure. While, as expected, due to increasing delocalization, the magnetic moment decreases upon increasing pressure, a sudden drop in moment was observed at the B-II–B-III transition from a moment substantially larger than 3 μ_B to a value smaller than 3 μ_B but substantially larger than 2 μ_B. We note that a high-spin-to-low-spin transition of an octahedrally coordinated Cr^{2+} ion would amount to a jump of moment m from 4 $\mu_B < m < 3$ μ_B to 2 $\mu_B < m < 1$ μ_B. Taking into account the covalency effect, the change in magnetic moment of Cr thus needs to be interpreted as a valence transition from a nominal 2+ valence state to a 3+ valence state [cf. insets in Fig. 6(b)], as opposed to the spin-state transition observed for $FePS_3$ and $MnPS_3$. This is further supported by the Bader charge analysis, which shows a jump at the B-II–B-III transition, with a sudden decrease in charge at the Cr site. To cross-check our conclusion of valence change, we considered two well-known compounds, CrS and Cr_2S_3, having a nominal Cr valence of 2+ and 3+, respectively. This would lead to Cr in d^4 and d^3 states. The computed Bader population of Cr was found to be 5.18 for CrS and 4.90 for Cr_2S_3. This is in good comparison with a Bader population of 5.11 in phase B-II and 4.88 in phase B-III of $CrPS_3$ at 20 GPa, confirming the change of valence state of Cr between phase B-II and phase B-III.

3. *Microscopic origin of the valence transition of Cr*

In order to understand the origin of the valence transition of Cr in $CrPS_3$, we focus on the electronic structure of the P_2S_6 molecular unit. The molecular orbitals of the P_2S_6 cluster create covalent P-S and P-P bonds. Their hybridization with Cr atomic orbitals, in turn, determines the electronic state of Cr. In Fig. 7(a), the pressure evolution of the P-P bond length in $CrPS_3$ is plotted, which shows an ∼8% increase at P_{c2}. To investigate the influence of this bond length change, we computed the partial densities of electronic states for s and

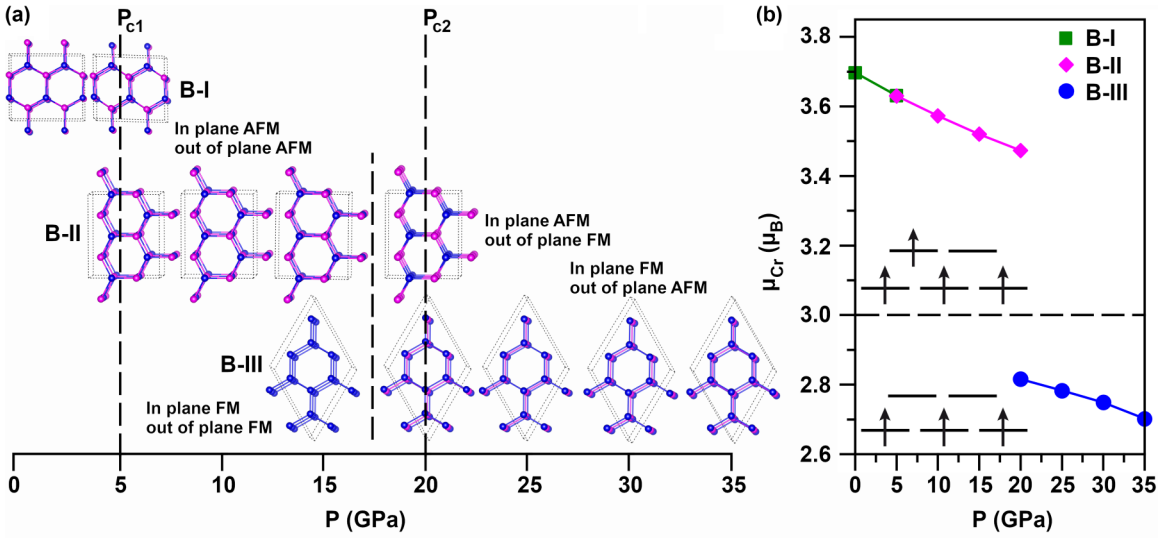

FIG. 6. (a) Evolution of the calculated lowest-energy magnetic structures of $CrPS_3$ as a function of pressure. The two different colors of the balls represent the up and down directions of Cr spin. Marked are the critical pressure values, the corresponding crystallographic phases, and the magnetic configurations. (b) The magnetic moment at the Cr site, plotted as a function of pressure. A jump is observed at $P = 20$ GPa, corresponding to a change in the nominal valence of Cr from 2+ to 3+ (shown as insets).

p orbitals of phosphorus in phases B-I and B-III. The spatial electron density distribution for the related energy states reflects the nature of the P-P and P-S bonds. As is evident from the electronic density plots in phase B-I, high electronic density is observed at the middle of the P-P bond, signaling P-P dimerization. This bonding nature drastically changes in phase B-III, exhibiting weakening of the P-P bond and accumulation of charges at P and S. While the P-P dimerization leads to stabilization of an effective charge state of 4− of the molecular unit (P_2S_6), in the absence of it, in the ionic bonding approach, the charge states 2− for sulfur ions and 4+ for phosphorus ions are expected, leading to a nominal 6− charge of (P_2S_6) instead of 4−. This, in turn, causes a change in the nominal oxidation state of Cr from 2+ to 3+.

This brings us to the question of why, upon application of pressure, two different routes are followed by $CrPS_3$ and

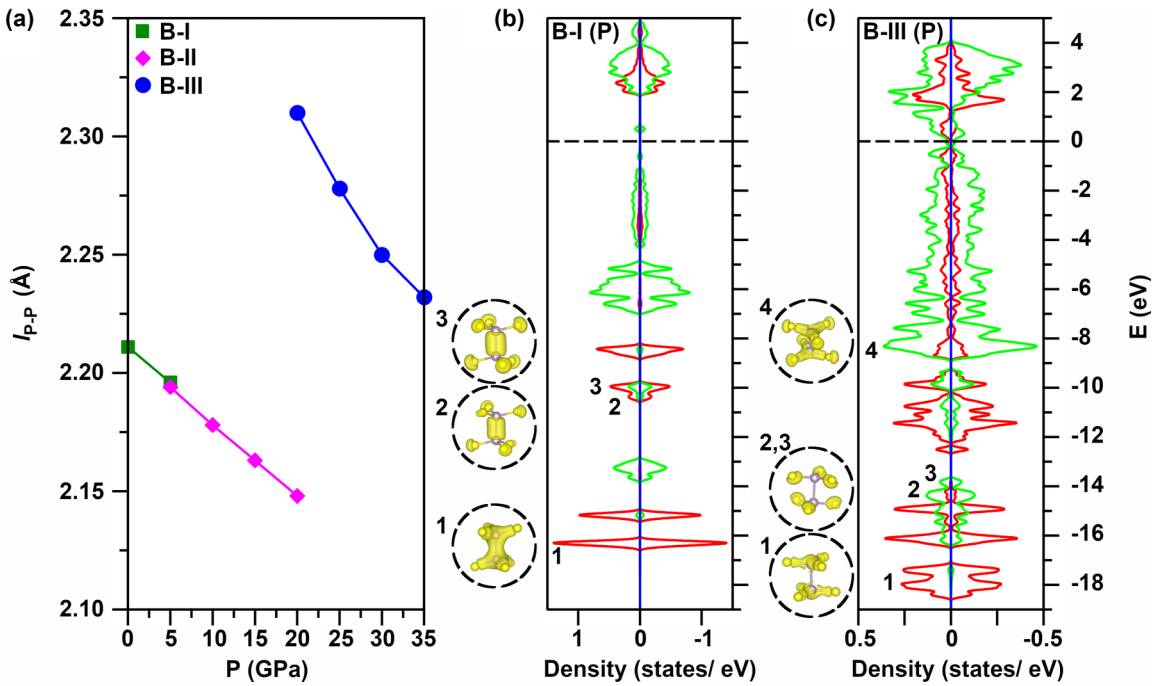

FIG. 7. (a) Evolution of P-P bond length in the $CrPS_3$ crystal structure as a function of pressure. The data points correspond to the most stable crystal structures at each pressure. (b) The partial densities of states, projected to P-S (red) and P-P (green), and space distribution of electron density (shown within encircled regions corresponding to the enumerated energy states) for the molecular orbitals of the P_2S_6 cluster.

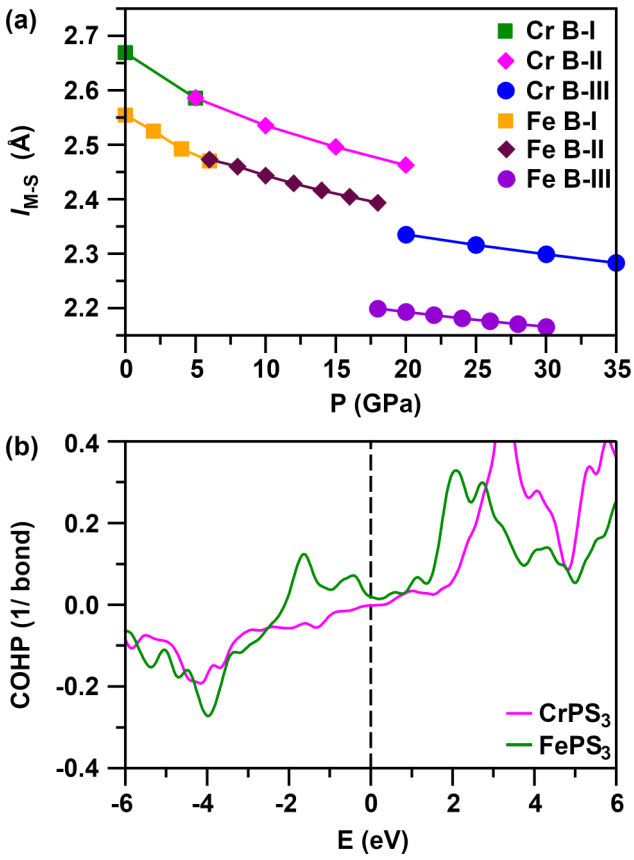

FIG. 8. (a) Comparison of M-S bond length in $CrPS_3$ and $FePS_3$ plotted as a function of pressure. (b) M-S COHP for $CrPS_3$ in comparison to that of $FePS_3$. The zero of the energy is set at the Fermi level.

$FePS_3$, one showing valence transition and another showing the spin-state transition. The clue to this is the Cr-S covalency compared with Fe-S covalency. Figure 8(a) shows the pressure variation of the M-S bond length in $CrPS_3$ compared with $FePS_3$. As is seen from the plot, the Cr-S bond length is about 4% larger than the Fe-S bond length in phases B-I and B-II, while it is about 7% larger in phase B-III. This hints towards weaker M-S covalency in $CrPS_3$ compared with that in $FePS_3$, as expected for an early transition metal in comparison to a late transition metal. In order to explicitly check this, we further computed the crystal orbital Hamiltonian population (COHP) [40], which is the density of states weighted by the corresponding Hamiltonian matrix elements. This permits energy-resolved analysis of pairwise interactions between atoms, providing the strength and nature of a bonding (negative COHP) or antibonding (positive COHP) interaction. Figure 8(b) shows the calculated COHP between M and S atoms, for $CrPS_3$ and $FePS_3$. $CrPS_3$ is found to exhibit weaker COHP compared with $FePS_3$, confirmed by the energy integrated value of the COHP until the Fermi level, which resulted in a value of 1.0 for $CrPS_3$ compared with a value of 1.5 for $FePS_3$. The S atoms are shared between M and P. Thus weakening of the M-S bond results in strengthening of the P-S bond, and vice versa. Strengthening of the P-S bond, in turn, weakens or destabilizes the P-P dimerization, as observed for $CrPS_3$. The situation may be compared with the case of FeO_2 versus FeS_2 [21]. In spite of sharing the same crystal structure of FeS_2, FeO_2 exhibits strikingly different electronic and magnetic properties. The oxidation state of the Fe ion in FeO_2 is argued to be not 2+, as in FeS_2, but close to 3+, which happens due to destabilization of ligand-ligand dimerization in oxides compared with sulfides. Similar to the situation of $CrPS_3$ compared with $FePS_3$, this is driven by weaker covalency between Fe and $2p$ O, compared with Fe and $3p$ S.

IV. SUMMARY AND OUTLOOK

To summarize, using the combination of an evolutionary genetic algorithm and first-principles calculations, we explore the pressure-induced changes in structural, electronic, and magnetic properties of the early-transition-metal-based, phosphorous trisulfide compound $CrPS_3$. The evolutionary algorithm, as implemented in USPEX, uncovered two high-pressure phases, with critical transition pressures of $P_{c1} \sim 5$ GPa and $P_{c2} \sim 20$ GPa. The symmetry of the high-pressure phases is found to be the same as that found for $FePS_3$. An indirect-band-gap-to-direct-band-gap transition happens at P_{c1}, and an insulator-to-metal transition happens at P_{c2}. Interestingly, the high-pressure phase above 20 GPa shows easy-axis, in-plane ferromagnetic ordering of Cr spins, opening up the possibility of stabilization of 2D ferromagnetism. The associated Cr magnetic moment shows a sharp drop at P_{c2}, found to be associated with the change of oxidation state of Cr from 2+ to 3+. The origin of this valence state transition turns out to be the pressure-induced destabilization of P-P dimerization, helped by the relatively weaker Cr-S covalency compared with that in late-transition-metal-based, phosphorous trisulfides such as $FePS_3$. This provides an explanation for the observed valence transition as opposed to the spin-state transition observed for $FePS_3$ and $MnPS_3$.

We note that while the synthesis of $CrPSe_3$ has been reported, the synthesis of $CrPS_3$ has not yet been reported; instead, synthesis of a related compound, $CrPS_4$, has been reported. Examination of the structure of $CrPS_4$ [41] shows that each P atom is connected to four S atoms, instead of three as in the MPX_3 structure. This means that each P atom is in the center of a tetrahedral molecular geometry surrounded by S atoms, with no direct bonding between neighboring P atoms. As argued above, weaker Cr-S covalency causes destabilization of the P-P dimer; thus $CrPS_4$ becomes a competing phase to $CrPS_3$. Replacement of S by Se enhances the Cr-X covalency, stabilizing the P-P dimerization and the $CrPX_3$ phase. The synthesis of $CrPS_3$ thus is possible if formation of the competing phase $CrPS_4$ can be avoided, since the $CrPS_3$ compound shows both good thermal stability and good dynamical stability. Chemical vapor transport (CVT) is the most frequently used technique to synthesize these crystals [42]. However, in recent times [43], the hydrothermal synthesis of metal oxides, followed by a step in a chemical vapor deposition (CVD) tubular furnace with stoichiometric quantities of S and P, has been demonstrated for transition metal phosphorous trisulfides, which may be a more promising route. The stabilization of the high-pressure easy-axis, ferromagnetic phase should encourage exploration of synthesis of $CrPS_3$.

ACKNOWLEDGMENTS

D.S. and T.S.-D. acknowledge the computational support of the Thematic Unit of Excellence on Computational Materials Science, funded by Nano Mission of the Department of Science and Technology. T.S.-D. acknowledges the J. C. Bose National Fellowship (Grant No. JCB/2020/000004) for funding.

[1] K. Khan, A. K. Tareen, M. Aslam, R. Wang, Y. Zhang, A. Mahmood, Z. Ouyang, H. Zhang, and Z. Guo, Recent developments in emerging two-dimensional materials and their applications, J. Mater. Chem. C **8**, 387 (2020).

[2] C. Gong, L. Li, Z. Li, H. Ji, A. Stern, Y. Xia, T. Cao, W. Bao, C. Wang, Y. Wang, Z. Q. Qiu, R. J. Cava, S. G. Louie, J. Xia, and X. Zhang, Discovery of intrinsic ferromagnetism in two-dimensional van der Waals crystals, Nature (London) **546**, 265 (2017).

[3] B. Huang, G. Clark, E. Navarro-Moratalla, D. R. Klein, R. Cheng, K. L. Seyler, D. Zhong, E. Schmidgall, M. A. McGuire, D. H. Cobden, W. Yao, D. Xiao, P. Jarillo-Herrero, and X. Xu, Layer-dependent ferromagnetism in a van der Waals crystal down to the monolayer limit, Nature (London) **546**, 270 (2017).

[4] H. Xu, S. Xu, X. Xu, J. Zhuang, W. Hao, and Y. Du, Recent advances in two-dimensional van der Waals magnets, Microstructures **2**, 2022011 (2022).

[5] T. Kong, K. Stolze, E. I. Timmons, J. Tao, D. Ni, S. Guo, Z. Yang, R. Prozorov, and R. J. Cava, VI_3—a new layered ferromagnetic semiconductor, Adv. Mater. **31**, 1808074 (2019).

[6] G. Le Flem, R. Brec, G. Ouvard, A. Louisy, and P. Segransan, Magnetic interactions in the layer compounds MPX_3 (M = Mn, Fe, Ni; X = S, Se), J. Phys. Chem. Solids **43**, 455 (1982).

[7] L. D. Casto, A. J. Clune, M. O. Yokosuk, J. L. Musfeldt, T. J. Williams, H. L. Zhuang, M.-W. Lin, K. Xiao, R. G. Hennig, B. C. Sales, J.-Q. Yan, and D. Mandrus, Strong spin-lattice coupling in $CrSiTe_3$, APL Mater. **3**, 041515 (2015).

[8] Y. Deng, Y. Yu, Y. Song, J. Zhang, N. Z. Wang, Z. Sun, Y. Yi, Y. Z. Wu, S. Wu, J. Zhu, J. Wang, X. H. Chen, and Y. Zhang, Gate-tunable room-temperature ferromagnetism in two-dimensional Fe_3GeTe_2, Nature (London) **563**, 94 (2018).

[9] M. M. Otrokov, I. P. Rusinov, M. Blanco-Rey, M. Hoffmann, A. Yu. Vyazovskaya, S. V. Eremeev, A. Ernst, P. M. Echenique, A. Arnau, and E. V. Chulkov, Unique Thickness-Dependent Properties of the van der Waals Interlayer Antiferromagnet $MnBi_2Te_4$ Films, Phys. Rev. Lett. **122**, 107202 (2019).

[10] S. Manzeli, D. Ovchinnikov, D. Pasquier, O. V. Yazyev, and A. Kis, 2D transition metal dichalcogenides, Nat. Rev. Mater. **2**, 17033 (2017).

[11] G. Ouvrard, R. Brec, and J. Rouxel, Structural determination of some MPS_3 layered phases (M = Mn, Fe, Co, Ni and Cd), Mater. Res. Bull. **20**, 1181 (1985).

[12] R. Brec, Review on structural and chemical properties of transition metal phosphorous trisulfides MPS_3, Solid State Ionics **22**, 3 (1986).

[13] H.-J. Koo, R. Kremer, and M.-H. Whangbo, Unusual spin exchanges mediated by the molecular anion $P_2S_6^{4-}$: theoretical analyses of the magnetic ground states, magnetic anisotropy and spin exchanges of MPS_3 (M = Mn, Fe, Co, Ni), Molecules **26**, 1410 (2021).

[14] M. J. Coak, D. M. Jarvis, H. Hamidov, C. R. S. Haines, P. L. Alireza, C. Liu, S. Son, I. Hwang, G. I. Lampronti, D. Daisenberger, P. Nahai-Williamson, A. R. Wildes, S. S. Saxena, and J.-G. Park, Tuning dimensionality in van-der-Waals antiferromagnetic Mott insulators $TMPS_3$, J. Phys.: Condens. Matter **32**, 124003 (2020).

[15] C. R. S. Haines, M. J. Coak, A. R. Wildes, G. I. Lampronti, C. Liu, P. Nahai-Williamson, H. Hamidov, D. Daisenberger, and S. S. Saxena, Pressure-Induced Electronic and Structural Phase Evolution in the van der Waals Compound $FePS_3$, Phys. Rev. Lett. **121**, 266801 (2018).

[16] Y. Wang, J. Ying, Z. Zhou, J. Sun, T. Wen, Y. Zhou, N. Li, Q. Zhang, F. Han, Y. Xiao, P. Chow, W. Yang, V. V. Struzhkin, Y. Zhao, and H.-K. Mao, Emergent superconductivity in an iron-based honeycomb lattice initiated by pressure-driven spin-crossover, Nat. Commun. **9**, 1914 (2018).

[17] H. Cui, S. Yun, K. J. Lee, C. Lee, S. H. Chang, Y. Lee, H. H. Lee, K. Raju, K. Moovendaran, R. Sankar, and K.-Y. Choi, Quasihydrostatic versus nonhydrostatic pressure effects on the electrical properties of $NiPS_3$, Phys. Rev. Mater. **5**, 124008 (2021).

[18] Y. Wang, Z. Zhou, T. Wen, Y. Zhou, N. Li, F. Han, Y. Xiao, P. Chow, J. Sun, M. Pravica, A. L. Cornelius, W. Yang, and Y. Zhao, Pressure-driven cooperative spin-crossover, large-volume collapse, and semiconductor-to-metal transition in manganese(II) honeycomb lattices, J. Am. Chem. Soc. **138**, 15751 (2016).

[19] S. Xu, Z. Wu, Y. Dedkov, and E. Voloshina, Adsorption of water on the pristine and defective semiconducting 2D $CrPX_3$ monolayers (X: S, Se), J. Phys.: Condens. Matter **33**, 354001 (2021).

[20] Q. L. Pei, X. Luo, G. T. Lin, J. Y. Song, L. Hu, Y. M. Zou, L. Yu, W. Tong, W. H. Song, W. J. Lu, and Y. P. Sun, Spin dynamics, electronic, and thermal transport properties of two-dimensional $CrPS_4$ single crystal, J. Appl. Phys. **119**, 043902 (2016).

[21] S. S. Streltsov, A. O. Shorikov, S. L. Skornyakov, A. I. Poteryaev, and D. I. Khomskii, Unexpected 3+ valence of iron in FeO_2, a geologically important material lying "in between" oxides and peroxides, Sci. Rep. **7**, 13005 (2017).

[22] G. Kresse and J. Hafner, *Ab initio* molecular dynamics for liquid metals, Phys. Rev. B **47**, 558 (1993).

[23] G. Kresse and J. Furthmuller, Efficient iterative schemes for *ab initio* total-energy calculations using a plane-wave basis set, Phys. Rev. B **54**, 11169 (1996).

[24] P. E. Blöchl, Projector augmented-wave method, Phys. Rev. B **50**, 17953 (1994).

[25] J. P. Perdew, K. Burke, and M. Ernzerhof, Generalized Gradient Approximation Made Simple, Phys. Rev. Lett. **77**, 3865 (1996).

[26] S. L. Dudarev, G. A. Botton, S. Y. Savrasov, C. J. Humphreys, and A. P. Sutton, Electron-energy-loss spectra and the structural stability of nickel oxide: An LSDA+U study, Phys. Rev. B **57**, 1505 (1998).

[27] S. Grimme, Semiempirical GGA-type density functional constructed with a long-range dispersion correction, J. Comput. Chem. **27**, 1787 (2006).

[28] A. Togo and I. Tanaka, First principles phonon calculations in materials science, Scr. Mater. **108**, 1 (2015).

[29] A. Togo, First-principles phonon calculations with phonopy and phono3py, J. Phys. Soc. Jpn. **92**, 012001 (2023).

[30] W. G. Hoover, Canonical dynamics: equilibrium phase-space distributions, Phys. Rev. A **31**, 1695 (1985).

[31] A. R. Oganov and C. W. Glass, Crystal structure prediction using *ab initio* evolutionary techniques: principles and applications, J. Chem. Phys. **124**, 244704 (2006).

[32] A. O. Lyakhov, A. R. Oganov, H. T. Stokes, and Q. Zhu, New developments in evolutionary structure prediction algorithm USPEX, Comput. Phys. Commun. **184**, 1172 (2013).

[33] A. R. Oganov, A. O. Lyakhov, and M. Valle, How evolutionary crystal structure prediction works – and why, Acc. Chem. Res. **44**, 227 (2011).

[34] S. Kirklin, J. E. Saal, B. Meredig, A. Thompson, J. W Doak, M. Aykol, S. Rühl, and C. Wolverton, The Open Quantum Materials Database (OQMD): assessing the accuracy of DFT formation energies, npj Comput. Mater. **1**, 15010 (2015).

[35] D. Lançon, H. C. Walker, E. Ressouche, B. Ouladdiaf, K. C. Rule, G. J. McIntyre, T. J. Hicks, H. M. Rønnow, and A. R. Wildes, Magnetic structure and magnon dynamics of the quasi-two-dimensional antiferromagnet $FePS_3$, Phys. Rev. B **94**, 214407 (2016).

[36] A. R. Wildes, B. Roessli, B. Lebech, and K. W. Godfrey, Spin waves and the critical behaviour of the magnetization in $MnPS_3$, J. Phys.: Condens. Matter **10**, 6417 (1998).

[37] D. Lançon, R. A. Ewings, T. Guidi, F. Formisano, and A. R. Wildes, Magnetic exchange parameters and anisotropy of the quasi-two-dimensional antiferromagnet $NiPS_3$, Phys. Rev. B **98**, 134414 (2018).

[38] See Supplemental Material at http://link.aps.org/supplemental/10.1103/PhysRevMaterials.7.064008 for details of spin arrangements and GGA+U+D2 computed total energies of different FM and AFM configurations.

[39] A. I. Liechtenstein, V. I. Anisimov, and J. Zaanen, Density-functional theory and strong interactions: Orbital ordering in Mott-Hubbard insulators, Phys. Rev. B **52**, R5467 (1995).

[40] R. Dronskowski and P. E. Blöchl, Crystal orbital Hamilton populations (COHP): energy-resolved visualization of chemical bonding in solids based on density-functional calculations, J. Phys. Chem. **97**, 8617 (1993); F. Boucher and R. Rousseau, Bonding and electronic properties of Cs_3Te_{22}, Inorg. Chem. **37**, 2351 (1998).

[41] Q. Chen, Q. Ding, Y. Wang, Y. Xu, and J. Wang, Electronic and magnetic properties of a two-dimensional transition metal phosphorous chalcogenide $TMPS_4$, J. Phys. Chem. C **124**, 12075 (2020).

[42] M. A. Susner, M. Chyasnavichyus, M. A. McGuire, P. Ganesh, and P. Maksymovych, Metal thio- and selenophosphates as multifunctional van der Waals layered materials, Adv. Mater. **29**, 1602852 (2017); F. Wang, T. A. Shifa, P. Yu, P. He, Y. Liu, F. Wang, Z. Wang, X. Zhan, X. Lou, F. Xia, and J. He, New frontiers on van der Waals layered metal phosphorous trichalcogenides, Adv. Funct. Mater. **28**, 1802151 (2018).

[43] F. Wang, T. A. Shifa, P. He, Z. Cheng, J. Chu, Y. Liu, Z. Wang, F. Wang, Y. Wen, L. Liang, and J. He, Two-dimensional metal phosphorus trisulfide nanosheet with solar hydrogen-evolving activity, Nano Energy **40**, 673 (2017); J. Chu, F. Wang, L. Yin, L. Lei, C. Yan, F. Wang, Y. Wen, Z. Wang, C. Jiang, L. Feng, J. Xiong, Y. Li, and J. He, High-performance ultraviolet photodetector based on a few-layered 2D $NiPS_3$ nanosheet, Adv. Funct. Mater. **27**, 1701342 (2017).